

Monitoring ion beam therapy with a Compton Camera: simulation studies of the clinical feasibility

J.-L. Ley¹, D. Dauvergne³, M. Fontana¹, N. Freud²,
J. Krimmer¹, J. M. Létang², V. Maxim², M.-H. Richard¹, and
É. Testa¹

¹Univ Lyon, Université Claude Bernard Lyon 1, CNRS/IN2P3, Institut de Physique Nucléaire de Lyon, 69622 Villeurbanne, France

²Univ Lyon, INSA-Lyon, Université Claude Bernard Lyon 1, UJM-Saint Étienne, CNRS, Inserm, Centre Léon Bérard, CREATIS UMR 5220 U1206, F-69373, Lyon, France

³LPSC, Université Grenoble-Alpes, CNRS/IN2P3 UMR5821, F-38026 Grenoble, France

E-mail: jeanluc.ley@gmail.com

Abstract.

The need of a treatment monitoring method in particle therapy, ideally in real-time, is becoming critical for a larger spread of this treatment technique. The ClaRyS French collaboration is developing a Compton camera prototype based on silicon detectors and BGO scintillator blocks. The present work aims at discussing the clinical applicability of this design by means of Monte Carlo simulations. The Compton camera performances have been studied for different configurations: the system absolute efficiency, studied with a preliminary irradiation via point-like monoenergetic sources, varies in the range $[1, 4] \times 10^{-4}$ with energy variations in the prompt gamma energy range and source position shifts of 300 mm in both direction with respect to the center of the camera. After this preliminary analysis, the detector have been set in realistic treatment conditions, with a PMMA cylindrical phantom exposed to proton and carbon ion beams at different intensities. The number of detected coincidences related to various beam time structure shows that a beam intensity reduction is needed with respect to standard clinical intensity in order to allow a proper monitoring functionality, without had-hoc filtering; two different event reconstruction methods have been compared, one based on analytical calculation with a line-cone technique, the second relying on an iterative MLEM algorithm. Both methods showed the possibility to reconstruct the beam depth-dose profile and to retrieve the dose fall-off with millimeter precision on a spot basis in a reduced beam intensity scenario.

Submitted to: *Phys. Med. Biol.*

Keywords: Compton Camera, ion therapy, clinical applicability, Prompt gamma

Contents

| | | |
|----------|--|-----------|
| 1 | Introduction | 3 |
| 2 | Material and methods | 7 |
| 2.1 | Simulation setup | 7 |
| 2.2 | Data treatment | 9 |
| 2.2.1 | Time structure and treatment | 9 |
| 2.2.2 | Data selection: time and energy cuts | 11 |
| 2.3 | Reconstruction algorithm | 12 |
| 2.3.1 | Line-cone algorithm | 12 |
| 2.3.2 | LM-MLEM algorithm | 13 |
| 2.4 | Precision estimation | 14 |
| 3 | Results | 17 |
| 3.1 | Compton camera absolute efficiency | 17 |
| 3.2 | Beam intensity | 19 |
| 3.3 | Compton camera precision: comparaison LM-MLEM vs Line cone reconstruction | 21 |
| 4 | Discussion | 24 |

1. Introduction

Ion beam therapy is a cancer treatment technique which is rapidly gaining importance in the global tumor therapy panorama. In addition to the already operational 70 clinical facilities, for more than 175000 patients already treated by the end of 2017, several new centers have been designed and approved for construction worldwide [Particle Therapy Cooperative Group, 2017]. The favorable feature of this treatment technique is connected to the peculiar energy deposition profile of charged particles as a function of depth in matter. As first observed by Bragg [Bragg and Kleeman, 1904], the depth-dose profile of charged particles shows a maximum close to the end of their range in matter; in addition to this, a strong enhancement of the relative biological effectiveness (RBE - capability of inducing DNA damages at fixed dose) is observed for ions heavier than protons in the region of the Bragg peak [Elsässer et al., , Weyrather et al., 1999], which enables a reduction of the biological dose in healthy tissues.

The Bragg peak position corresponds to the maximum of the dose deposited in the patient and must be tuned to cover the target volume and, at the same time, spare the surrounding healthy tissues. The tumor volume is defined via CT scan in the standard clinical routine, and the treatment is planned via treatment planning software. In human body, the exploitation of the high ballistic precision of ion beams is strongly limited by treatment planning and delivery uncertainties, like uncertainties in the material composition determination, CT units conversion to ion stopping power, patient mispositioning, organ motion or morphological changes between treatment fractions (a standard treatment is divided into several fractions over several weeks, according to the tumor and patient characteristics). These uncertainties force the clinicians to fix relatively large safety margins around the planned treatment volume, up to 3.5% + 3 mm [Paganetti, 2012]. The research and clinics community agrees on the fact that ion-range verification is one of the conditions (at present the main condition) required for a broader usage of ion beam therapy and for its further development. With the goal of fully exploiting the ion beam therapy dosimetric potential, the monitoring should be in real-time and ideally in 3 dimensions, in order to be able to interrupt the treatment in case of severe issues, corresponding to important differences between the planned and delivered dose to the target volume or to surrounding organs, in particular in case of proximity to organs-at-risk (OAR).

Several techniques have been considered worldwide for twenty years. Most of the studied techniques rely on the detection of secondary radiations generated during the slowing down process of incident ions, in particular during nuclear reactions. Among theses secondary radiations, positron emitters have been deeply studied in order to exploit positron emission tomography (PET) machines for treatment monitoring. PET techniques are based on the detection of the two back-to-back 511 keV photons produced by the annihilation of positrons (created by the emitter fragments of nuclear reactions) with patient electrons, resulting in a delayed radiation which should be detected with

time coincidences, allowing for an intrinsic background reduction. Nevertheless, the monitoring with positron emitters secondary signal must deal with a limited count rate compared to medical imaging PET, with the lifetime of emitters providing a delayed information that implies the signal integration over a whole treatment fraction (not a single spot or group of spots), with physiological washout effects depending on to the emitters lifetime.

Even if the only available and functional range monitoring system in a clinical center is based on this technique [Enghardt et al., 2004], several clinical experience with commercial or adapted PET system already shown intrinsic limitations mainly connected to the ring geometry (not directly applicable to the treatment monitoring due to the presence of the beam) or in general to geometrical constraints limiting the field of view and the resulting system global efficiency and spatial accuracy (the limited detection angle generates artifacts in the final image) [Parodi, 2016]. The research is ongoing and new results are expected for the next years thanks to the introductions of new systems with adapted geometries, to the improvements in acquisition and reconstruction techniques and to the clinical introduction of time-of-flight systems, intrinsically able to improve the detector spatial resolution via interaction time information, and depth-of-interaction reconstruction, which will allow for a more precise spatial reconstruction for reduced angular artifacts effects.

In addition to positron annihilation products, a different kind of photons is emitted during ion irradiation. They emerge from the relaxation of excited nuclei in a wide energy range, between some hundreds of keV till about 8-10 MeV. After the first idea proposal published in 2003 [Stichelbaut and Jongen, 2003], these secondary products of particle treatment have been deeply investigated and the correlation of this gamma radiation to the ion depth-dose profile has been confirmed by several research groups, starting from [Min et al., 2006] for protons and [Testa et al., 2008] for heavier ions (mainly carbon). The so-called prompt gamma-rays (PG) have the advantage to be emitted almost instantaneously after the beam interaction in the tissue, making them more adapted than PET 511 keV gammas for real-time monitoring. Consequently, different techniques have been proposed to exploit this signal for treatment monitoring purpose, with the related detection systems. Some methods are based on PG timing [Golnik et al., 2014, Krimmer et al., 2017a] or energy [Verburg and Seco, 2014] information and rely on non-collimated systems; more complex detection apparatus can achieve an actual PG imaging, by exploiting mechanical or electronic collimation (i.e. with collimated gamma camera or Compton camera, respectively) for the photon selection (see e.g. [Min et al., 2006, Bom et al., 2012, Smeets et al., 2012, Roellinghoff et al., 2014, Priegnitz et al., 2015, Frandes et al., 2010, Llosá et al., 2012, Kormoll et al., 2011, McCleskey et al., 2015, Matsuoka, 2015, Peterson et al., 2010, Solevi et al., 2016, Aldawood et al., 2017]). For a review on PG monitoring, see [Krimmer et al., 2017b]

Originally designed for astrophysics applications, the potential of Compton cameras for medical imaging has been soon recognized [Todd et al., 1974] and

then directly translated to the ion beam therapy monitoring domain. Such a gamma detection system is generally composed of two sections: a scatterer and an absorber. The scatterer is dedicated to the gamma Compton scattering, and should be so adapted in order to optimize the Compton scattering probability in the prompt gamma energy range, while reducing the so called Doppler broadening effect due to electron bounding and motion [Ordonez et al., 1997]; this leads, in most of the cases, to the choice of a light material (low Z), segmented in several subsections. However, when efficiency has to be privileged, heavier materials may be used ([Solevi et al., 2016, Aldawood et al., 2017, Polf et al., 2015]). The absorber is devoted to the final absorption of the Compton scattered photons via photoelectric effect; it is often composed of segmented high- Z scintillating materials. Slightly different Compton camera configuration can also achieve Compton electron tracking in the scattering detector [Frandes et al., 2010, Yoshihara et al., 2017], which results in additional information for the further reconstruction algorithm. The collected interaction positions and energy depositions in the two detector sections are used to limit the emission point on the surface of a cone (or to a segment in the cone if the Compton electron track information is retrieved), via Compton kinematics reported in equation 1 (for an electron initially at rest):

$$\cos \theta = 1 - \frac{m_e c^2 E_1}{E_2(E_1 + E_2)}, \quad (1)$$

where $m_e c^2 = 511$ keV, E_1 and E_2 are the energies, respectively, deposited in the scatterer and the absorber. Once the cones are calculated, analytic or iterative algorithms are used to create the image of the prompt gamma emission distribution, with intrinsic 3 dimensional capability [McKisson et al., 1994, Kuchment and Terzioglu, 2016].

Several sources of uncertainty and signal background are connected to this detection method. Considering a gamma interacting twice in the detector, i.e. once in the scatterer and once in the absorber, a complete photon energy absorption is needed since the initial photon energy (E_1) is not known a priori and the reported formula assumes valid the relation in equation 2:

$$E_0 = E_1 + E_2. \quad (2)$$

An underestimation of the total initial energy (caused by a photon non-complete absorption in the absorber section or by the Compton electron escape from the scatterer section), leads to an underestimation of the Compton angle, so to a Compton cone reconstruction incertitude. For a three-interaction operating mode (making use of double scattered photons), the initial photon energy can be calculated analytically so that a complete absorption is not mandatory. In addition to this, the Compton kinematics formula does not take into account the initial bounding configuration of the Compton scattering electron, which creates a blur in the Compton angle reconstruction, resulting in the already cited Doppler broadening effect [Ordonez et al., 1997]. Furthermore, the time structure of the incoming particles

plays an important role due to the detection principle, which is based on time coincidences between the two detector sections. The final image accuracy then suffers from false coincidences, generated by two prompt gammas interacting in the same time window or by the contamination of different kind of secondaries, mainly neutrons and protons. It is clear that excellent detector time resolution can limit the amount of random coincidences, as well as different background rejection methods can be applied to select real coincidences [Draeger et al., 2017]. Energy selections can be applied to the collected coincidences [Polf et al., 2009, Hilaire et al., 2016], or the homogeneous neutron background can be reduced via time-of-flight information [Testa et al., 2010].

A French collaboration of 4 research institutions (Institut de Physique Nucleaire and Centre de Recherche en Acquisition et Traitement de l'Image pour la Santé in Lyon, Laboratoire de Physique Subatomique et Cosmologie in Grenoble, Centre de Physique des Particules in Marseille) is focused on the design and development of gamma detectors for online ion beam therapy monitoring. The project includes the development and clinical test of a Compton camera prototype based on semiconductor and scintillator detectors [Krimmer et al., 2015]; the feasibility of its clinical application is studied in this work with Monte Carlo simulations.

In a previous study by Ortega and colleagues [Ortega et al., 2015] a detailed analysis of the noise sources for Compton imaging in proton therapy monitoring is presented, and the clinical application of this method for detecting range shifts is tested. The simulation study, performed with a simple Compton camera prototype composed by multiple LaBr_3 layers with a ideal mono-energetic proton beam impinging on a PMMA phantom, showed the relative expected rate of prompt gammas and neutrons, and the resulting rate of random coincidences ranging from 19 % to more than 60 % depending on the beam energy and the coincidence time window. This amount of fake events leads to complex reconstruction scenarios, where the identification of a 3 mm range shift is not clear for all cases.

Starting from these results, the ClaRyS camera performances are here studied as a function of the gamma energy in the prompt gamma energy range, and the possible application of this detector as depth-dose profile monitor during ion beam therapy clinical treatment is analyzed by investigating the effect of the beam time structure on the rate of true and random coincidences, as well as on the background level. After a preliminary study with point-like gamma sources irradiation focused on detector efficiency measurements as a function of the source position and gamma energy, clinical proton and carbon beams impinging on an homogeneous PMMA phantom are simulated to reproduce treatment conditions and analyze the prompt gamma detection resulting scenario. A beam intensity reduction with respect to treatment intensities is studied for monitoring purpose, with the aim of increasing the ratio between true and random coincidence events: the maximum beam rate tolerance is here estimated. Two kinds of reconstruction algorithms, a line-cone analytic method and a MLEM iterative one, are applied to the collected data in order to compare the imaging results. Finally, the Compton camera precision in the identification of the dose profile fall-off is reported.

2. Material and methods

2.1. Simulation setup

The monitoring system modeled in this simulation work is a Compton camera prototype under development within the French collaboration CLaRyS. The detectors detailed characteristics can be found in [Krimmer et al., 2015]. A scheme of the simulation setup is given in figure 1.

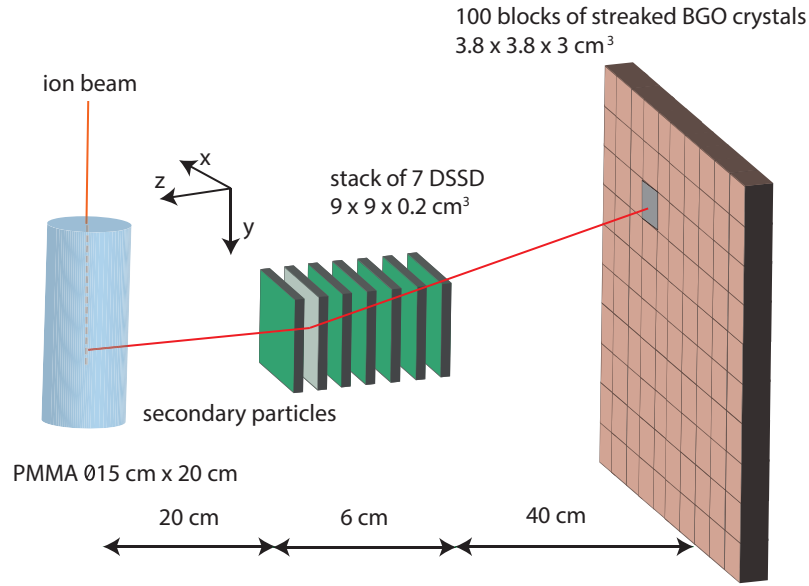


Figure 1: Scheme of the simulation setup: a PMMA cylindrical phantom is set in front of the Compton camera prototype. The Compton camera is composed of a stack of 7 double sided silicon strip detectors (scatterer) and a plan of 100 single BGO blocks. The set distances are realistic for clinical conditions. This geometrical configuration has been used for all the simulations presented in this work.

Like most of the Compton camera devices, the CLaRyS prototype includes a scatterer and an absorber. The scatterer consists of seven parallel planes of silicon detectors (double-sided silicon strip detectors, DSSDs), $9 \times 9 \times 0.2 \text{ cm}^3$, with 1 cm distance between the centers of two neighboring planes, while the absorber is composed of an array of 10×10 BGO (Bismuth Germanate - Bi_2GeO_7) blocks ($3.5 \times 3.5 \times 3.0 \text{ cm}^3$ each) placed at 40 cm from the last silicon layer (center-to-center distance). The ion beam interacts with a cylindrical PMMA (PolyMethylMethAcrylate) phantom (15 cm diameter and 20 cm length) placed in front of the Compton camera as target. It is placed 20 cm far from the first silicon plane (center-to-center distance) in order to fit with realistic clinical conditions.

The silicon detectors have a strip pitch of 1.4 mm, for a total of 64 strips per side (double-sided readout based on electron and hole pairs collection). The strips

are not reproduced in the simulation code, and the transverse spatial resolution is set to 0.9 mm FWHM at the reference energy of 1 MeV, according to preliminary measurements performed on smaller detector prototypes. Concerning the parallel direction, the interaction position is set to the center of the involved silicon plane.

Regarding the BGO blocks, their entrance surface is streaked in a 8×8 matrix of pseudo-pixels, 4.4 mm^2 side, and the readout is performed via 4 photo-multiplier tubes. The position reconstruction is achieved via Anger logic for the real detector, but a mono-block crystal is simulated here for simplicity. The events are selected to be limited to a single block component based on spatial analysis, and the interaction position is reconstructed via center of gravity calculation if multiple interaction occur. An incertitude contribution, randomly extracted by a Gaussian of 5 mm FWHM, is added to the reconstructed position to fit with the geometrical features. For what concerns the parallel direction, given the fact that the employed BGO blocks have not depth of interaction reconstruction capabilities, the interaction position is fixed to the center of the mono-block crystal.

Preliminary characterization measurements allowed to estimate the energy resolution of the BGO blocks, which is accordingly set to 17% FWHM at the reference energy of 667 keV (a 137-cesium source has been used for the measurements). The energy resolution of the silicon detector is set to 2.3 keV (RMS) according to the design expectations; no characterization data are yet available for an instrumental estimate.

The time resolution has been set to 3.0 ns FWHM for the BGO blocks and to 15.0 ns FWHM for the silicon slabs, according to preliminary measurements performed on test detector modules at the GANIL center in France.

The detector resolutions play an important role in the Compton camera performances. The absorber spatial resolution influences the position of the apex of the Compton cone, as well as its axis orientation. The scatterer energy resolution determines the Compton cone aperture angle. The time resolution impacts the coincidence window between the absorber and the scatterer, and so its true/random coincidence discrimination capabilities.

The CLaRyS project also includes the development of a beam tagging hodoscope, composed of scintillating fibers read out by multi-channel photomultipliers. This detector is used to synchronize the beam time and space structure to the prompt gamma detection in order to tune the detection window reducing the background contamination. This detector section is not included in the simulation, but its time resolution has to be taken into account for the time-of-flight discrimination. It is set to 1 ns FWHM. The detectors spatial, energy and time resolutions are summarized in table 1.

The Monte Carlo simulation study is performed with the Geant4 toolkit, version 9.6 patch 02. Geant4 has been developed at CERN for high energy physics experiments, but it has been shown that it can be used for ion beam therapy studies [Cirrone et al., 2011, Toshito et al., 2010]. However, some improvements are still needed in order to extend the hadronic models to low energy applications [Dedes et al., 2014, Pinto et al., 2016].

The particle interactions in matter are described in this work by means of different

Table 1: Estimations of reachable resolutions with the detectors. Those resolutions are applied during the simulations.

| Resolution (FWHM) at 1 MeV | Scatterer | Absorber | Hodoscope |
|----------------------------|-----------|----------|-----------|
| spatial [mm] | 0.9 | 5 | 1 |
| energy | 2.3 keV | 17 % | / |
| timing [ns] | 15 | 3 | 1 |

models, listed in table 2. Additionally, the Doppler broadening and the photon polarization effects are taken into account.

Table 2: Hadronic models used in the Geant4 simulations.

| Process | Protons | Ions | Neutrons |
|-------------------------|-----------------|---|--|
| Electromagnetic | | | |
| Inelastic | G4BinaryCascade | G4QMDReaction (G4IonsShenCrossSection) | standard _{option3} G4BinaryCascade + G4NeutronHPInelastic (<19 MeV) |
| Elastic | G4LElastic | G4LElastic | G4LElastic + G4NeutronHPElastic (<19 MeV) |
| Fission | / | / | G4LFission + G4NeutronHPFission(<19 MeV) |
| Capture | / | / | G4LCapture + G4NeutronHPCapture (<19 MeV) |
| Radioactivedecay | / | G4Radioactivedecay | / |

The two main beam particles used in clinics are considered in this work: protons and carbon ions. The beam range of interest is 15.2 cm in the PMMA phantom, and the associated energy is 160 MeV for protons and 305 MeV/n for carbon ions.

In order to reproduce a realistic clinical beam, the beam transverse dimension is modeled with a Gaussian distribution with a standard deviation of 5 mm for protons at 160 MeV and 3.5 mm for carbon ions at 305 MeV/n. The Compton camera setup does not change for the different incident particles. The beam intensity for a spot in pencil beam scanning (PBS) mode for protons is 10^8 particles and 10^5 particles for carbon ions. The beam time structure is applied in the data analysis stage, described below.

2.2. Data treatment

2.2.1. Time structure and treatment Two different beam time structures have been considered for this study, related to two kinds of accelerators used in clinical practice: the IBA C230 cyclotron for protons (used in 16 clinical centers worldwide) and the Heidelberg (Germany) synchrotron installed in the Ion Therapy Center (HIT) for carbon ions. Even if the beam microstructure changes depending on the ion energy and the beam intensity, the microstructure is modeled according to the reported features at a specific energy and intensity for simplicity. For protons at 160 MeV, the primary particles are grouped in bunches of 2 ns (this value may vary also according to the distance between the cyclotron and the treatment room, and energy spread selection)

at a frequency of 106 MHz (9.42 ns) [F Roellinghoff, 2014]. The clinical beam intensity is 3.2 nA which corresponds to about 200 protons per bunch. Concerning the carbon ion beam at 305 MeV/u, the estimated microstructure is composed of 30 ns duration bunches at a frequency of 5.9 MHz (170 ns period). The clinical beam intensity for carbon ions is 5×10^7 ions/s, corresponding to about 9 ions per bunch. This beam structure is extrapolated from measurements performed by our group in 2013 at HIT; the beam time structure was measured for 200 MeV/u and 400 MeV/u primary ion energy with a two-fiber hodoscope (basic prototype of the one at present under development) and the spill signal was given by the accelerator. Figure 2 shows the beam structure for carbon ions at 400 MeV/u. The pulses have a spill period of 150.2 ns and each bunch is approximately 21.5 ns. The mentioned measurements have shown that the spill phase changes during the extraction: this implies that the HF signal from the synchrotron can not be used to trigger the pulses, so that the use of an additional beam time stamp system like the hodoscope seems required for time-of-flight background rejection purposes.

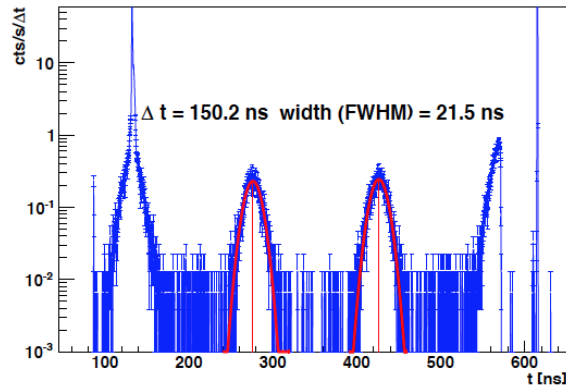


Figure 2: Time micro-structure measured from a carbon ion beam at 400 MeV/u delivered at HIT. The pulses have an extraction period of 150.2 ns and the bunches are 21.5 ns FWHM. The measurement was achieved with a two-scintillating-fiber hodoscope.

The coincidence window (between scatterer and absorber events) is set to 40 ns, centered on each absorber detected interaction. This value is adapted to the detectors time resolutions. Table 3 summarizes the presented beam time structures and coincidence reconstruction features.

Table 3: Description of the two beam structures studied: the IBA cyclotron C230 for protons and the synchrotron installed at the Heidelberg Ion Therapy Center (HIT) in Germany for carbon ions. The macro-structure of the synchrotron, at the second time scale, is not considered here. The beam structures are applied to the simulation data.

| Clinical features | Facility Clinical intensity Energy | Protons | Carbon ions |
|-------------------|---|------------------------|------------------------|
| | | IBA Cyclotron C230 | Synchrotron at HIT |
| Beam structure | Bunch time [ns] | 2×10^{10} p/s | 5×10^7 ions/s |
| | Period [ns] | 160 MeV | 305 MeV/u |
| | Primaries /bunch | 3.2 | 30 |
| | Time resolution [ns] | 9.4 | 170 |
| Detectors | Coincidence window [ns] | 217 | 9 |
| | Time resolution [ns] | 40 | 40 |
| | | Si: 15 and BGO: 3 | |

2.2.2. Data selection: time and energy cuts As already explained in the introduction, the Compton detection principle is based on a double interaction in the scatterer and absorber section, where an interaction is defined as an energy deposit in a detector module. As discussed in section 2.2.1, the coincidence reconstruction relies on a defined time window, fixed according to the involved detector resolution. In a simulation environment, different kinds of coincidences events can be distinguished and studied:

- real coincidences: created by a single photon first interaction in a single scatterer plane and then in a single absorber block;
- quasi-simultaneous interaction from two secondary particles;
- double interaction from the same particle different from a gamma.

In a real clinical environment there is no way to select the real coincidences, so that the collected data are affected by a certain number of the so-called random coincidences. The amount of random coincidences depends on the detector time resolutions, on the fixed time coincidence window and on the beam time structure, for fixed beam energy, phantom composition and camera prototype setup. In figure 3 a schematic view of the different kinds of coincidences is presented.

In addition to this, the prompt gamma measurement is contaminated by other secondary particles produced by the beam interaction with the patient/phantom, mainly massive and charged particles (protons, neutrons). As already mentioned, it has been demonstrated by our group that a time-of-flight discrimination is possible and effective in reducing this source of background. In fact, the photons are moving at the speed of light while the massive particles approach the detector at a lowest speed. The time information coming from the hodoscope and from the absorber can be then combined to fix a detection time window and reject all the events outside the window. In this work, the time between the incident particle creation and the secondary particle detection in the absorber is considered as the time-of-flight. The hodoscope time resolution $u_{hodoscope}$ (1 ns FWHM) is applied to the primary particle creation time, with a contribution

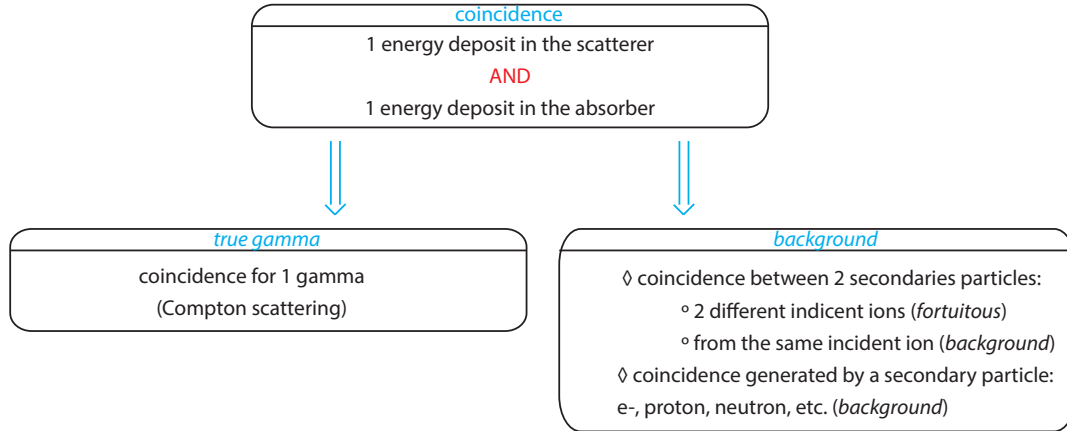


Figure 3: Diagram showing the different definitions of coincidences in the Compton camera.

randomly extracted from a Gaussian with $\sigma = 1/2.35$ ns, while the detection time in the absorber is affected by the absorber time resolution.

$$TOF_{theoretical} = t_{absorber} - t_{hodoscope} \quad (3)$$

$$TOF_{simulation} = t_{absorber} + t_{creation} + u_{hodoscope} \quad (4)$$

The time-of-flight spectrum resulting from the simulation shows that the coincidences of interest (produced by prompt-gamma rays) are included in a window between 0 and 6 ns (figure 4). Therefore, all the coincidences with a TOF higher than 6 ns have been rejected, reproducing a possible clinical background rejection scenario.

In addition to the time-of-flight based selection, energy thresholds are also defined for the event detection. On a single detector basis, 50 keV is set as lower threshold for the silicon layers and 100 keV for the absorber. On a complete event basis, a total absorbed energy lower limit is set to 1 MeV.

2.3. Reconstruction algorithm

Once the coincidences are defined and selected according to the fixed physical cuts, the prompt-gamma emission point has to be reconstructed for each event. This can be done via analytic or iterative algorithms based on the Compton kinematics (see section 1), presented in the following sections.

2.3.1. Line-cone algorithm The reconstruction via line-cone algorithm exploits the energy deposit and position information collected by the camera in addition to the beam path information. Thanks to the deposited energies in the detectors and the interaction positions, a cone surface is analytically defined via the Compton equation 1. We assume that the initial energy of the gamma ray is fully absorbed in the absorber. This hypothesis, combined to the detector energy resolutions, leads to a potential

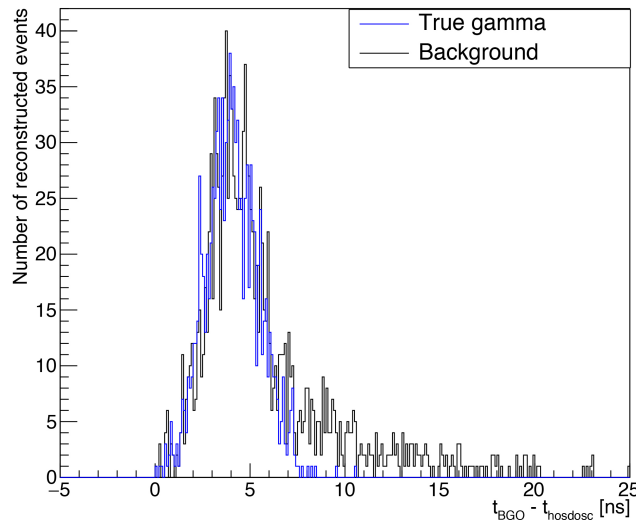


Figure 4: Time of flight spectrum obtained by means of the simulation for a proton beam at 160 MeV and 1×10^8 incident protons. The detection time for the absorber is given by the tag for the first deposit energy. The blue curve represents the time of flight for true events and the black one represents the background.

uncertainty on the cone aperture. The interaction position in the scatter gives the cone apex and the line connecting the interaction position in scatterer and absorber gives the cone axis. In order to simplify the reconstruction, the beam direction is used to limit the possible solutions (laying on the reconstructed cone surface) to two points (intersection of the beam direction and the reconstructed cone). The set of all the reconstructed points gives the emission source distribution. The obtained final image is then the 2 dimensional projection of the prompt gamma emission spectrum.

2.3.2. LM-MLEM algorithm The iterative methods allow to get a 3D image reconstruction, potentially by taking into account the spatial resolution and the energy resolution of the detectors. Few iterative algorithms have been developed for Compton event reconstruction. [Schone et al., 2010, Zoglauer et al., 2011, Gillam et al., 2011, Mackin et al., 2012, Lojacono et al., 2013].

The *List-Mode Maximum Likelihood Expectation Maximization* (LM-MLEM) algorithm is a MLEM version which allows to free from sinograms and to reconstruct the image directly from the list of detected events. The first step is to define the volume which includes the origin of the prompt gamma ray detected. This volume is divided into equal voxels and the emission intensity is assumed homogeneous for each voxel j , with a Poisson distribution of parameter λ_j (a vector of the emissions intensities of all the voxels). The algorithm is based on a system matrix T composed of the coefficients t_{ij} which represent the probability that a photon produced in the voxel j is detected in coincidence by the Compton camera as an event i . The probability for a gamma

detected in coincidence to be emitted from the voxel j is denoted as s_j . The LM-MLEM algorithm starts with an initial value $\lambda^{(0)}$, which can be the simple back-projection reconstruction. The iterations rely on the following recurrence relation:

$$\lambda_j^{(l+1)} = \frac{\lambda_j^{(l)}}{s_j} \sum_{i=1}^{N_\gamma} t_{ij} \frac{1}{P_i^{(l)}}, \quad \text{with} \quad P_i^{(l)} = \sum_{k=1}^{N_v} t_{ik} \lambda_k^{(l)}, \quad (5)$$

where N_γ is the number of detected events and N_v is the number of voxels in the image.

The LM-MLEM algorithm used for this study is the one developed by the CREATIS research group in Lyon [Maxim, 2014, Hilaire et al., 2014].

For each photon detected, the system matrix T is calculated by taking into account the uncertainties on the angle between the source and the involved scatterer plane and the angle between the scatterer plane and the absorber involved module. The matrix elements t_{ij} are calculated as:

$$t_{ij} = K(\beta_i, E_{tot}) \frac{|\cos(\theta_{\vec{V}_2 \vec{V}_1})|}{V_2 V_1^2} \int_{M \in v_j} \frac{|\cos(\theta_{\vec{V}_1 \vec{M}})|}{V_1 M^2} h_i(M) dv, \quad (6)$$

where β_i is the Compton scattering angle, V_1 the interaction position in the scatterer, V_2 the interaction position in the absorber, h_i the spatial kernel which models the uncertainties on the Compton angle for each voxel M , $K(\beta_i, E_{tot})$ the differential cross section and v the reconstructed volume.

In order to simplify and speed up the calculation of the t_{ij} matrix, the voxels located far from the reconstructed cone are set to 0. The distance between the cone and the voxel is calculated by taking the voxel center as reference point. The spatial resolutions are not included in this version of the algorithm.

For each iteration, the matrix T is stored and the reconstructed image can be produced via a Matlab simple interface.

2.4. Precision estimation

The camera precision is defined as the difference between the expected Bragg peak position (according to the treatment planning) and the Bragg peak position reconstructed through the data. This is a critical parameter which will be used to fix a decision threshold during a ion beam treatment.

In this study a reference profile has been defined as the reconstructed emission vertex profile at high statistics, via analytic (line cone) and iterative (LM-MLEM) algorithms; this will be used to mimic the treatment planning. This Bragg peak position is compared to the ones reconstructed at lower statistics (close to clinical conditions) via analytic and iterative algorithms.

The high statistic profile has been obtained with 2×10^{10} incident protons (figure 5a) for the line-cone reconstruction and with 1×10^{10} incident protons (figure 5b) for the LM-MLEM reconstruction method. The *SmoothKern* method, with the Nadaraya-Watson

regression, is used to smooth the reference profiles in order to reduce relative statistic fluctuations.

A region of interest (ROI) ranging from $y = 0$ mm to $y = +100$ mm is defined around the expected Bragg peak position, located at $y = +50$ mm in the phantom. The reference profiles are modelled in the ROI by a linear combination named Non-Uniform Rational Basis Splines (NURBS).

A new independent profile should be simulated at low statistics for the precision calculation. However, with the aim to speed up the analysis, a random extraction from the NURBS profile (5c and 5d) is performed following the Poisson law, in order to select reduced data sets. The desired low statistics ranges from 10^8 to 5×10^9 incident protons.

The minimal distance between the NURBS reference profile and the low statistic reconstructed profiles is estimated thanks to the χ^2 method. For the χ^2 estimate, the low statistics profile is defined around the fall-off position from $y = +30$ mm to $y = +70$ mm. The minimization process tests the profiles at low statistics on a 60 mm variation range, between -30 mm and $+30$ mm with respect to the initial position, with a step of 0.1 mm. The χ^2 is calculated as follows:

$$\chi^2 = \sum_{i=1} (y_{sample,i} - y_{NURBS,i})^2, \quad (7)$$

where y_{sample} is the number of coincidences for the low statistics profile, y_{NURBS} is the number of coincidences for the reference profile NURBS (scaled at the same low statistic) and i the step number.

The global minimum of all the reconstructed profiles is then retrieved. The figures 5e and 5f show the distribution of χ^2 calculated for a low statistic profile at 10^8 incident protons.

A total of a thousand profiles at the low statistic are generated (named realizations) and the χ^2 minimization is applied to each of them. The standard deviation of the distribution resulting of the thousand results gives the precision of the camera for a given number of incident protons. The figure 5g and 5h show the distributions at 10^8 incident protons for the line-cone and LM-MLEM algorithms.

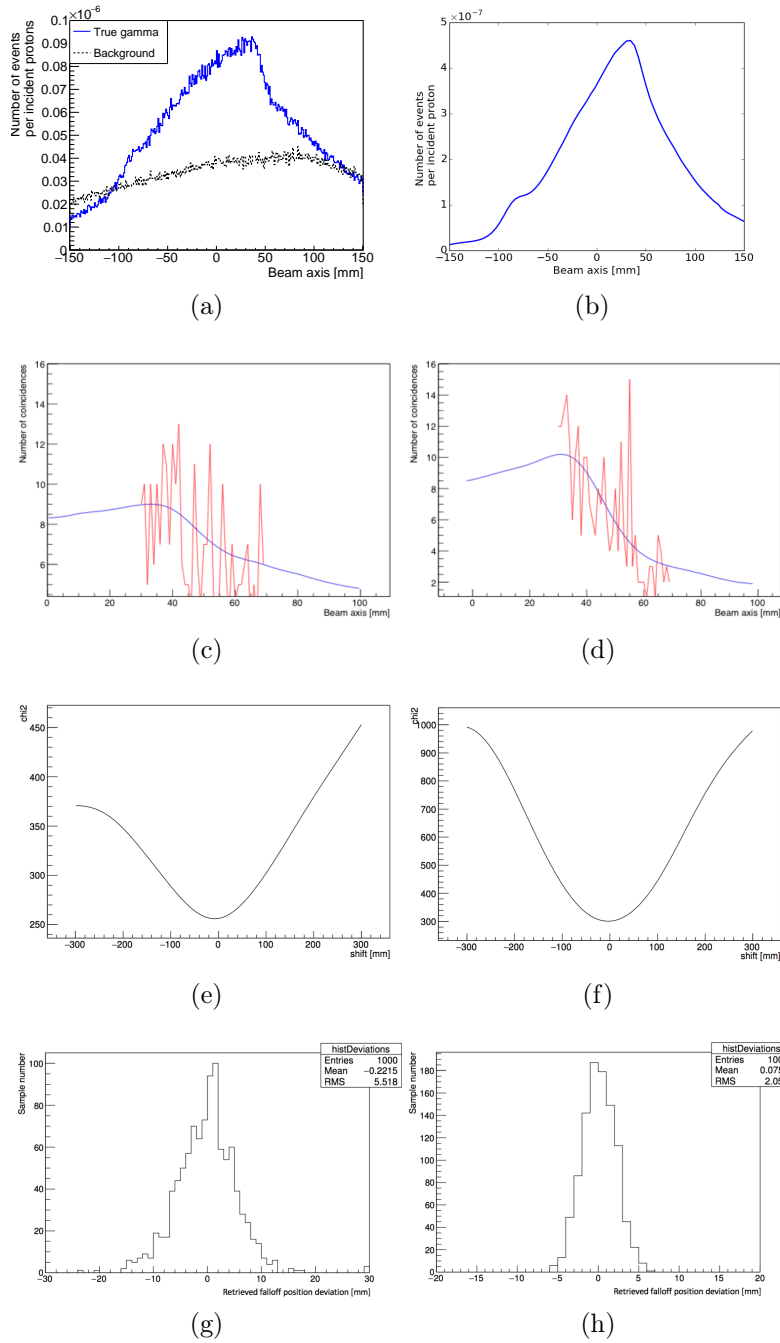


Figure 5: Treatment comparison for the same proton simulation with the line cone algorithm (left column: figures 5a, 5c, 5e, 5g) and the LM-MLEM algorithm (right column: figures 5b, 5d, 5f, 5h). The first row gives the reconstructed profile for 2×10^{10} incident protons (figure 5a) and for 1×10^{10} incident protons (figure 5b) respectively. The figures 5c and 5d are showing the reference curve (blue) and the estimated curve with Poisson's law at 1×10^8 incident protons. The figures 5e and 5f are the χ^2 minimization results for one realization. The minimum of the curve gives the best fit between the reference curve and the low statistics one. Finally, the figures 5g and 5h represents the results for 1000 χ^2 minimizations. The Compton camera precision is estimated thanks to the standard deviation of the distribution.

3. Results

In the following paragraphs the results of the simulation study are presented and discussed with constant reference to the possible clinical application of the CLaRyS Compton camera system as particle therapy monitor. The clinical implementation of such a monitoring system has been tested with the simulation of clinical proton and carbon ion beams, with realistic spatial and time structure reproducing two accelerators at present employed for treatments 2.2.1. As preliminary study, the detection efficiency of the camera has been tested with the simulation of the irradiation with point-like gamma sources in different position with respect to the center of the camera. After that, the beam exposure has been simulated with different beam intensities for an analysis of the clinical-like detection environment (background, random coincidence contamination), in order to focus in the end on the event reconstruction with the comparison of two different methods (line-cone analytical reconstruction and MLEM iterative algorithm) and on the estimate of the camera precision in the identification of the fall-off of the dose profile.

3.1. Compton camera absolute efficiency

The absolute efficiency is crucial for the Compton camera performances and for its possible application in treatment monitoring. As already mentioned in section 1, an efficient monitoring system should be ideally in real time, in order to allow for a treatment adaptation or interruption in case of severe issues detected in the delivered dose profile with respect to the planned treatment. In order to achieve an online detection of such deviations, given the reduced prompt gamma emission rate per incident ion [Ortega et al., 2015], an high detection efficiency is required to perform a monitoring on, ideally, a beam spot basis. In addition to this, the absolute detection efficiency directly affects the image reconstruction quality, which is in general increased for increased statistics.

In order to well define the expected camera efficiency, it has been studied with the irradiation from point-like monoenergetic gamma sources, set in different positions with respect to the center of the camera on the transverse plane.

The absolute efficiency ϵ is defined as:

$$\epsilon = \frac{N_{\gamma_{recons}}}{N_{\gamma_{total}}}, \quad (8)$$

with $N_{\gamma_{recons}}$ the number of gamma events in coincidences,

$N_{\gamma_{total}}$ the total number of gamma emitted: 10^8 .

The setup is the same as figure 1, with the exception of the PMMA phantom which is removed to leave the gamma source in air. The point source is set in the range -300 mm to $+300$ mm (with the center of the camera transverse section set in the position 0) with a step of 20 mm close to the center of the camera, then increasing

up to 1 cm for the most peripheral point. The movement followed the transverse axis of the camera. Different energies has been tested to mimic different prompt gamma spectroscopic lines: 300 keV, 500 keV, 1 MeV, 2 MeV, 4 MeV, 6 MeV.

The obtained results are shown in figure 6. On the left side, we show the results achieved with an ideal detector, while on the right side realistic energy cuts are applied on each detector section: the lower energy limit has been set to 50 keV for the scatterer and 100 keV for the absorber.

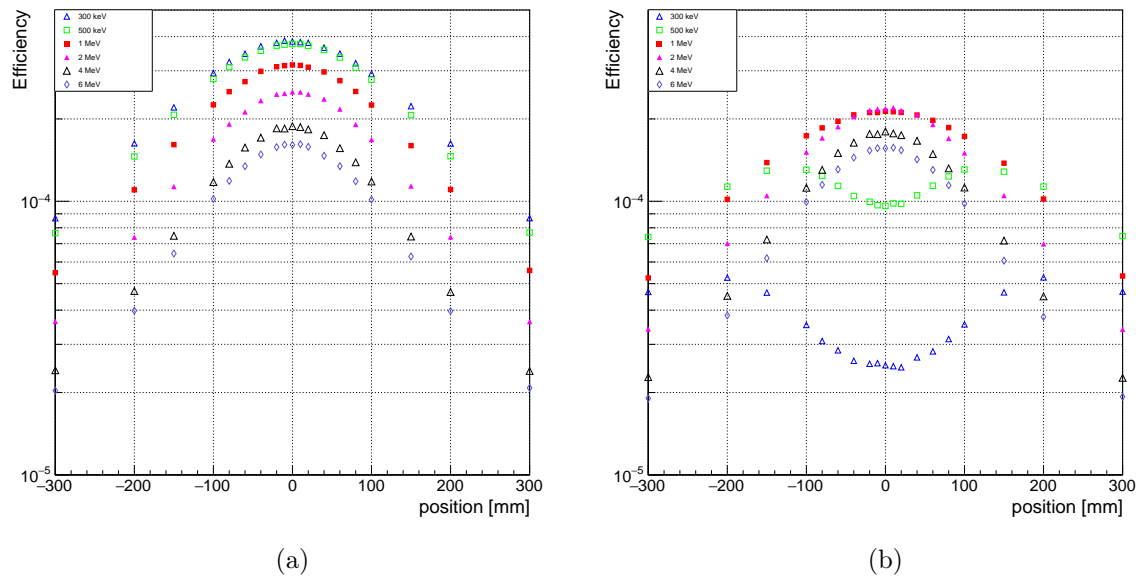


Figure 6: Absolute Compton camera efficiency as a function of the gamma source position for different gamma energies, in the range between 300 keV to 6 MeV. The left side shows the camera efficiency without any applied energy cut. It models an ideal Compton camera. In the right side, detector energy cuts are applied: the lower energy thresholds are set to 50 keV for the scatterer and 100 keV for the absorber, to reproduce realistic scenario. This values can change for the final detector configuration, according to the detector energy resolutions achieved.

As expected according to the interaction probability energy dependency, the efficiency is higher for low gamma energies, and it lies in the range 4×10^{-4} at 300 keV and 1.5×10^{-4} at 6 MeV (figure 6). Moreover, it can be noticed how the efficiency quickly drops quickly as the point source drifts away from the camera center: this effect is more important for high energies, for which the incident gamma is less deflected in the scatterer for the same energy deposited compared to a low energy gamma (see equation 1). Therefore, considering 1 MeV as the average and reference gamma energy for ion beam therapy monitoring, the Compton camera position optimization with respect to the expected Bragg peak position appears mandatory for an efficient fall-off reconstruction.

Regarding the applied energy cuts, figure 6(b) clearly shows an important effect on low energy gammas in the central area of the camera. The effect is negligible for positions with a distance greater than 200 mm from the center of the camera, and for any distance at energies above 2 MeV. A further study showed how this effect is mainly due to the cut applied on the scatterer detector. Indeed, for low energies, below 2 MeV, the increased efficiency in the central section of the camera active surface shown in figure 6(a) is linked to the increased relative number of photons approaching the camera with small angles. These photons are more likely undergoing Compton scattering with a reduced energy deposition, which is recorded by an ideal detector and rejected by the energy cut. The effect is all the more important as the primary gamma energy is limited, creating the peculiar energy dependence of the efficiency reduction emerged in the results in figure 6(b).

3.2. Beam intensity

As the Compton detection principle relies on time coincidences, in addition to the main importance played by the detectors energy resolutions, the beam intensity and time structure are important parameters to be studied in order to assess the possible clinical implementation of a Compton detection based monitoring of ion beam treatment. In the simulation, the beam intensity is modeled by an average number of particles per bunch. The exact number of particles in each bunch is given by a random extraction from a Poisson distribution, where the mean value is the selected beam intensity. The range of intensities is defined in order to cover a wide range of operation: from a very low beam intensity to a realistic, clinical particle rate. Therefore, for proton and carbon ions, the lowest beam intensity is set to 0.1 particles per bunch on average, while the upper limit is set to 217 protons or 70 carbon ions per bunch. For the analysis of the results, the coincidence yields are scaled to the number of incident ions and the beam intensity to the average number of ions per bunch.

In figure 7 the different components of the resulting secondary signal are shown as a function of the beam intensity. The true coincidences represent detector time coincidences generated by the same gamma ray. All the other coincidence types compose the background. All the simulations are performed with 10^8 primary protons and 2×10^5 primary carbon ions. Those values correspond to realistic clinical values used for the treatment of a single spot. The collected data sets are reported with and without the applied time-of-flight discrimination, mainly employed for neutron rejection, as mentioned in section 2.2.2.

In figure 7(a) and (b) the amount of true gamma coincidences and background events are reported before and after reconstruction (the reconstruction algorithms select the events according to the chosen reconstruction parameters) as a function of the beam intensity for proton (a) and carbon ion (b) beams. In addition to this, for each curve realized with the complete collected data set, the related one realized after time-of-flight selection of events is sketched. All the curves have been normalized to the

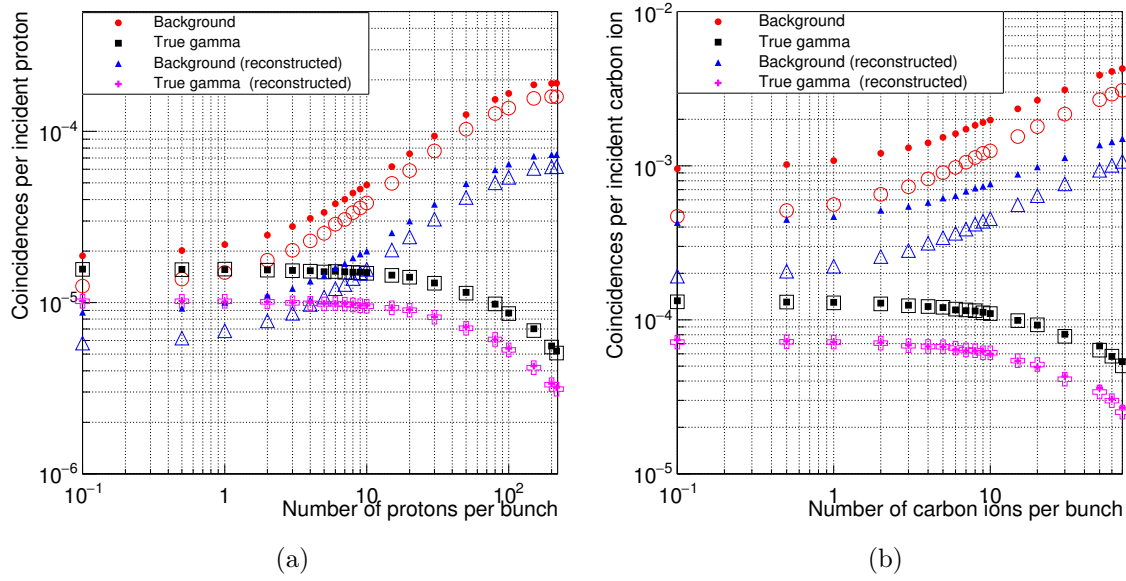


Figure 7: Coincidences yield for protons (left) and carbon ions (right) as a function of the beam intensity. The intensity is reported as number of incident particles per bunch. The filled markers correspond to the collected data without time-of-flight discrimination, while this cut is applied to the data reported with empty markers. Moreover, the yields are given before and after the profile reconstruction with the line cone algorithm.

number of incident ions.

As expected, the amount of background events (mainly random coincidences) increases with the increasing beam intensity: a factor of about 30 with respect to true gamma events is obtained for proton beams at clinical intensity (200 proton/bunch) with no event selection, while a factor more than two times higher is reported for carbon ions in the same conditions. Even if the time-of-flight selection can slightly improve this result by reducing the amount of background events, it is evident that such a beam intensity is not optimal for a proper monitoring. Furthermore, considering the rate of single interactions per detector, the results obtained by a preliminary analysis showed, as an example, a single rate of about 300 MHz on the absorber and 20 MHz on the first scatterer planes. These rates are not compatible with the detection rate capabilities of the detector read-out chains. As a result, it appears not possible to perform a valuable treatment monitoring with the CLaRyS Compton camera at a clinical beam intensity. Nevertheless, the monitoring objective becomes feasible in a reduced beam intensity scenario for proton irradiation. Figure 7(a) shows how the amount of true gamma events and background events becomes compatible at the intensity of about 1 proton per bunch. In the case of carbon ions, the larger amount of secondary neutron produced during the patient treatment seems to require other background rejection methods in order to lead to an advantageous signal-over-background ratio.

Given the results presented in this paragraph, in the following the attention will be focused on proton beams at reduced intensities, with the aim of comparing the line-cone reconstruction and the MLEM reconstruction algorithm and to estimate the camera fall-off identification precision.

3.3. Compton camera precision: comparaison LM-MLEM vs Line cone reconstruction

The simulation setup shown in figure 1 has been implemented to test the line-cone analytic reconstruction method and compare it to the iterative LM-MLEM algorithm developed in Lyon by the CREATIS group [Maxim, 2014, Hilaire et al., 2014]. A single data set has been collected, corresponding to the irradiation of the PMMA phantom with a proton 160 MeV monoenergetic beam, with a reduced intensity of 1 proton per bunch. A total of 10^{10} protons has been simulated to define the reference Bragg peak, and then different sub-data sets have been extracted for the precision estimate at different statistics, as explained in section 2.4. Figure 8 shows the results of the reconstruction of the data set obtained for the selection of 10^8 primary protons of 160 MeV, via the two reconstruction method already detailed before. To be noticed that the two reconstruction methods produce different results: the line-cone method is based on the beam direction information, so that it naturally produce a mono-dimensional image as result, while the MLEM method is able to reconstruct the prompt-gamma emission distribution in 3 dimensions. A projection along the beam direction is then extracted from the MLEM reconstructed image in order to allow a direct comparison.

Starting from the reference data set with 10^{10} primary protons, 11 subsets are extracted to mimic the dose profile falloff reconstruction for different primary particle statistics, in the range 1×10^8 to 5×10^9 . To be noticed that the delivered beam intensity is always of 1 proton per bunch, as a consequence of the results presented in section 3.2. The analysis method described in section 2.4 is applied to the different data set to retrieve the camera precision in the dose profile falloff identification. The results are shown in figure 9, where the two reconstruction methods are represented by different markers.

At the expense of an increased calculation time, the iterative MLEM reconstruction method allows to achieve a better precision, with a reduction of about 3 mm of the falloff retrieval precision in the whole range of statistics explored. A linear behavior, highlighted by the performed linear fit of the two data sets, is verified with increasing number of primary protons, starting from the single spot scale of about 10^8 primaries, till 5×10^9 protons, which can correspond to the monitoring of a group of spot with the same planned range. If we consider the important increase in the precision of the falloff identification given by the increased statistics, the spot grouping method seems to be promising for monitoring purpose when high accuracy is required, probably obtained

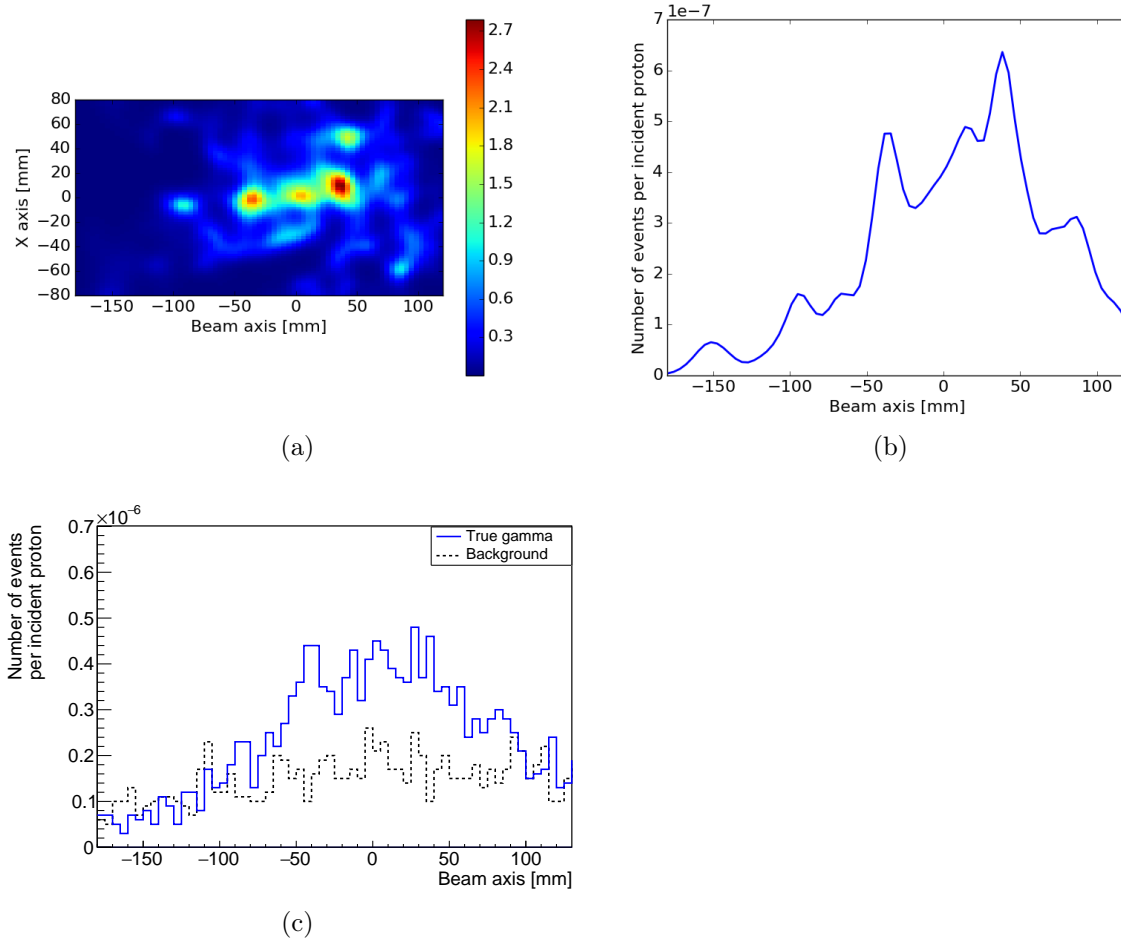
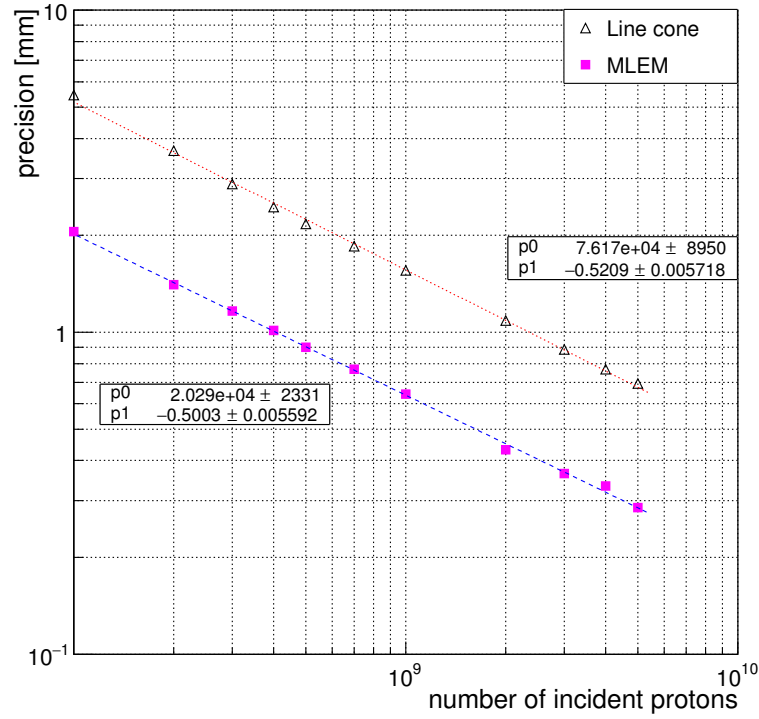


Figure 8: Line cone and LM-MLEM reconstruction for a 160 MeV proton beam, 10^8 total incident protons. The beam intensity is 1 proton per bunch. The Compton camera is centered at the expected Bragg peak position, $y = +50\text{mm}$. The time-of-flight event selection is applied on the collected data set. 20 iterations are performed for the MLEM reconstruction.

Figure (a) represents the MLEM reconstructed 2D image in the plan (x,y), parallel to the camera entrance surface. The position $x = 0\text{mm}$ corresponds to the center of the PMMA phantom and the y direction corresponds to the beam axis. In figure (b) the mono-dimensional profile along the y axis is sketched. The profile peak is located at $y = +50\text{mm}$. Figure (c) shows the profile obtained by means of line-cone algorithm for the same time-of-flight selected data.

in the post-treatment due to the long required reconstruction time. A sufficiently good precision is achieved on a spot basis, where the precision is about 2 mm with a MLEM reconstruction: a qualitative monitoring of each spot seems then possible. Given the long calculation time required by the MLEM algorithm, the line-cone reconstruction method, despite the reduced precision, can still be an option for on-line treatment check,

Figure 9: Compton camera precision for two different reconstruction algorithms: line-cone and LM-MLEM. The precision is shown as a function of the total number of incident protons, in the range 1×10^8 to 5×10^9 . A linear fit is realized on the results in order to obtain the slope of the results (p1 parameter in legend). A logarithmic scale is used on both axes.



when safety limit can be fixed in order to exclude severe deviation from the treatment planning and an interruption of the dose delivery in real time can be foreseen.

4. Discussion

DISCUSSION

Acknowledgments

This work is supported by the FP7-ENVISION program WP3, the FP7-ENTERVISION program, the FP7- ULICE program, the ANR Gamhadron project, the Rhone-Alpes Regional Program for Hadrontherapy Research, the MI2B GDR and the LabEx PRIMES.

References

- [Aldawood et al., 2017] Aldawood, S., Thirolf, P. G., Miani, A., Böhmer, M., Dedes, G., Gernhäuser, R., Lang, C., Liprandi, S., Maier, L., Marinšek, T., Mayerhofer, M., Schaart, D. R., Valencia Lozano, I., and Parodi, K. (2017). Development of a compton camera for prompt-gamma medical imaging. *Radiation Physics and Chemistry*, 140:190 – 197. 2nd International Conference on Dosimetry and its Applications (ICDA-2) University of Surrey, Guildford, United Kingdom, 3-8 July 2016.
- [Bom et al., 2012] Bom, V., Joulaeizadeh, J., and Beekman, F. (2012). Real-time prompt gamma monitoring in spot-scanning proton therapy using imaging through a knife-edge-shaped slit. *Physics in Medicine and Biology*, 57(2):297.
- [Bragg and Kleeman, 1904] Bragg, W. H. M. A. and Kleeman, R. (1904). Lxxiv. on the ionization curves of radium. *The London, Edinburgh, and Dublin Philosophical Magazine and Journal of Science*, 8(48):726–738.
- [Cirrone et al., 2011] Cirrone, G. P., Cuttone, G., Mazzaglia, S. E., Romano, F., Sardina, D., Agodi, C., Attili, A., Blancato, A. A., De Napoli, M., Di Rosa, F., and others (2011). Hadrontherapy: a Geant4-based tool for proton/ion-therapy studies. *Prog. Nucl. Sci. Technol*, 2:207–212.
- [Dedes et al., 2014] Dedes, G., Pinto, M., Dauvergne, D., Freud, N., Krimmer, J., Létang, J. M., Ray, C., and Testa, E. (2014). Assessment and improvements of Geant4 hadronic models in the context of prompt-gamma hadrontherapy monitoring. *Physics in Medicine and Biology*, 59(7):1747–1772.
- [Draeger et al., 2017] Draeger, E., Peterson, S., Mackin, D., Chen, H., Beddar, S., and Polf, J. C. (2017). Feasibility studies of a new event selection method to improve spatial resolution of compton imaging for medical applications. *IEEE Trans Radiat Plasma Med Sci*, 1(4):358–367.
- [Elsässer et al.,] Elsässer, T., Weyrather, W. K., Friedrich, T., Durante, M., Iancu, G., Krämer, M., Kragl, G., Brons, S., Winter, M., Weber, K.-J., and Scholz, M. Quantification of the relative biological effectiveness for ion beam radiotherapy: Direct experimental comparison of proton and carbon ion beams and a novel approach for treatment planning. *International Journal of Radiation Oncology Biology Physics*, 78(4):1177–1183.
- [Enghardt et al., 2004] Enghardt, W., Crespo, P., Fiedler, F., Hinz, R., Parodi, K., Pawelke, J., and Pönisch, F. (2004). Charged hadron tumour therapy monitoring by means of PET. *Nuclear Instruments and Methods in Physics Research Section A: Accelerators, Spectrometers, Detectors and Associated Equipment*, 525(1):284 – 288. Proceedings of the International Conference on Imaging Techniques in Subatomic Physics, Astrophysics, Medicine, Biology and Industry.
- [F Roellinghoff, 2014] F Roellinghoff, A. B. (2014). Real-time proton beam range monitoring by means of prompt-gamma detection with a collimated camera. *Physics in medicine and biology*, 59(5):1327–38.
- [Frandes et al., 2010] Frandes, M., Zoglauer, A., Maxim, V., and Prost, R. (2010). A tracking compton-scattering imaging system for hadron therapy monitoring. *IEEE Transactions on Nuclear Science*, 57(1):144–150.
- [Gillam et al., 2011] Gillam, J. E., Lacasta, C., Torres-Espallardo, I., Candela Juan, C., LlosÀa, G., Solevi, P., Barrio, J., and Rafecas, M. (2011). A Compton imaging algorithm for on-line monitoring in hadron therapy. volume 7961, pages 79611O–79611O–8.
- [Golnik et al., 2014] Golnik, C., Hueso-Gonzalez, F., Muller, A., Dendooven, P., Enghardt, W., Fiedler,

- F., Kormoll, T., Roemer, K., Petzoldt, J., Wagner, A., and Pausch, G. (2014). Range assessment in particle therapy based on prompt gamma-ray timing measurements. *Phys Med Biol*, 59(18):5399–5422.
- [Hilaire et al., 2014] Hilaire, E., Robert, C., Lojacono, X., Sarrut, D., Buvat, I., Peyrin, F., and Maxim, V. (2014). Compton imaging in proton therapy: reconstructed image of the simulated prompt- γ distribution. In *ICTR-PHE 2014*, page S43, Geneva, Switzerland.
- [Hilaire et al., 2016] Hilaire, E., Sarrut, D., Peyrin, F., and Maxim, V. (2016). Proton therapy monitoring by compton imaging: influence of the large energy spectrum of the prompt-gamma radiation. *Phys Med Biol*, 61(8):3127–3146.
- [Kormoll et al., 2011] Kormoll, T., Fiedler, F., Schöne, S., Wüstemann, J., Zuber, K., and Enghardt, W. (2011). A compton imager for in-vivo dosimetry of proton beams – A design study. *Nuclear Instruments and Methods in Physics Research Section A: Accelerators, Spectrometers, Detectors and Associated Equipment*, 626-627:114 – 119.
- [Krimmer et al., 2017a] Krimmer, J., Angellier, G., Balleyguier, L., Dauvergne, D., Freud, N., Hérault, J., Létang, J. M., Mathez, H., Pinto, M., Testa, E., and Zoccarato, Y. (2017a). A cost-effective monitoring technique in particle therapy via uncollimated prompt gamma peak integration. *Applied Physics Letters*, 110(15):154102.
- [Krimmer et al., 2017b] Krimmer, J., Dauvergne, D., Létang, J., and Testa, E. (2017b). Prompt-gamma monitoring in hadrontherapy: A review. *Nuclear Instruments and Methods in Physics Research Section A: Accelerators, Spectrometers, Detectors and Associated Equipment*.
- [Krimmer et al., 2015] Krimmer, J., Ley, J.-L., Abellan, C., Cachemiche, J.-P., Caponetto, L., Chen, X., Dahoumane, M., Dauvergne, D., Freud, N., Joly, B., Lambert, D., Lestand, L., Magne, M., Mathez, H., Maxim, V., Montarou, G., Morel, C., Pinto, M., Ray, C., Reithinger, V., Testa, E., and Zoccarato, Y. (2015). Development of a compton camera for medical applications based on silicon strip and scintillation detectors. *Nuclear Instruments and Methods in Physics Research Section A: Accelerators, Spectrometers, Detectors and Associated Equipment*, 787:98–101.
- [Kuchment and Terzioglu, 2016] Kuchment, P. and Terzioglu, F. (2016). 3D Image Reconstruction from Compton camera data.
- [Llosá et al., 2012] Llosá, G., Barrio, J., Cabello, J., Crespo, A., Lacasta, C., Rafecas, M., Callier, S., de La Taille, C., and Raux, L. (2012). Detector characterization and first coincidence tests of a compton telescope based on labr3 crystals and sipms. *Nuclear Instruments and Methods in Physics Research Section A: Accelerators, Spectrometers, Detectors and Associated Equipment*, 695:105 – 108. New Developments in Photodetection NDIP11.
- [Lojacono et al., 2013] Lojacono, X., Richard, M.-H., Ley, J.-L., Testa, E., Ray, C., Freud, N., Létang, J., Dauvergne, D., Maxim, V., and Prost, R. (2013). Low statistics reconstruction of the Compton camera point spread function in 3D prompt- γ imaging of ion beam therapy. *Nuclear Science, IEEE Transactions on*, 60(5):3355–3363.
- [Mackin et al., 2012] Mackin, D., Peterson, S., Beddar, S., and Polf, J. (2012). Evaluation of a stochastic reconstruction algorithm for use in Compton camera imaging and beam range verification from secondary gamma emission during proton therapy. *Physics in Medicine and Biology*, 57(11):3537–3553.
- [Matsuoka, 2015] Matsuoka, Y. (2015). Performance of a new electron-tracking Compton camera under intense radiations from a water target irradiated with a proton beam. *JINST*, 10(01):C01053.
- [Maxim, 2014] Maxim, V. (2014). Filtered backprojection reconstruction and redundancy in Compton camera imaging. *IEEE Transactions on Image Processing*, 23(1):332–341.
- [McCleskey et al., 2015] McCleskey, M., Kaye, W., Mackin, D. S., Beddar, S., He, Z., and Polf, J. C. (2015). Evaluation of a multistage cdznte compton camera for prompt γ imaging for proton therapy. *Nuclear Instruments and Methods in Physics Research Section A: Accelerators, Spectrometers, Detectors and Associated Equipment*, 785:163 – 169.
- [McKisson et al., 1994] McKisson, J. E., Haskins, P. S., Phillips, G. W., King, S. E., August, R. A., Piercey, R. B., and Mania, R. C. (1994). Demonstration of three-dimensional imaging with a

- germanium Compton camera. *IEEE Transactions on Nuclear Science*, 41(4):1221–1224.
- [Min et al., 2006] Min, C.-H., Kim, C. H., Youn, M.-Y., and Kim, J.-W. (2006). Prompt gamma measurements for locating the dose falloff region in the proton therapy. *Applied Physics Letters*, 89(18):183517.
- [Ordonez et al., 1997] Ordonez, C. E., Bolozdynya, A., and Chang, W. (1997). Doppler broadening and energy uncertainties in Compton cameras. *IEEE Nucl. Sci. Symp. Conf. Rec. 2 1361*–1365.
- [Ortega et al., 2015] Ortega, P. G., Torres-Espallardo, I., Cerutti, F., Ferrari, A., Gillam, J. E., Lacasta, C., Llosa, G., Oliver, J. F., Sala, P. R., Solevi, P., and Rafecas, M. (2015). Noise evaluation of compton camera imaging for proton therapy. *Phys Med Biol*, 60(5):1845–1863.
- [Paganetti, 2012] Paganetti, H. (2012). Range uncertainties in proton therapy and the role of monte carlo simulations. *Physics in Medicine and Biology*, 57(11):R99–R117.
- [Parodi, 2016] Parodi, K. (2016). On- and off-line monitoring of ion beam treatment. *Nuclear Instruments and Methods in Physics Research Section A: Accelerators, Spectrometers, Detectors and Associated Equipment*, 809:113 – 119. Advances in detectors and applications for medicine.
- [Particle Therapy Cooperative Group, 2017] Particle Therapy Cooperative Group, P. (2017). Ptcog stats. www.ptcog.ch.
- [Peterson et al., 2010] Peterson, S. W., Robertson, D., and Polf, J. (2010). Optimizing a three-stage compton camera for measuring prompt gamma rays emitted during proton radiotherapy. *Phys Med Biol*, 55(22):6841–6856.
- [Pinto et al., 2016] Pinto, M., Dauvergne, D., Freud, N., Krimmer, J., Létang, J. M., and Testa, E. (2016). Assessment of geant4 prompt-gamma emission yields in the context of proton therapy monitoring. *Frontiers in Oncology*, 6:10.
- [Polf et al., 2015] Polf, J. C., Avery, S., Mackin, D. S., and Beddar, S. (2015). Imaging of prompt gamma rays emitted during delivery of clinical proton beams with a compton camera: feasibility studies for range verification. *Physics in Medicine and Biology*, 60(18):7085.
- [Polf et al., 2009] Polf, J. C., Peterson, S., Ciangaru, G., Gillin, M., and Beddar, S. (2009). Prompt gamma-ray emission from biological tissues during proton irradiation: a preliminary study. *Phys Med Biol*, 54(3):731–743.
- [Priegnitz et al., 2015] Priegnitz, M., Helmbrecht, S., Janssens, G., Perali, I., Smeets, J., Vander Stappen, F., Sterpin, E., and Fiedler, F. (2015). Measurement of prompt gamma profiles in inhomogeneous targets with a knife-edge slit camera during proton irradiation. *Phys Med Biol*, 60(12):4849–4871.
- [Roellinghoff et al., 2014] Roellinghoff, F., Benilov, A., Dauvergne, D., Dedes, G., Freud, N., Janssens, G., Krimmer, J., Létang, J. M., Pinto, M., Prieels, D., Ray, C., Smeets, J., Stichelbaut, F., and Testa, E. (2014). Real-time proton beam range monitoring by means of prompt-gamma detection with a collimated camera. *Physics in Medicine and Biology*, 59(5):1327.
- [Schone et al., 2010] Schone, S., Shakirin, G., Kormoll, T., Herbach, C., Pausch, G., and Enghardt, W. (2010). A common approach to image reconstruction for different applications of Compton cameras. In *Nuclear Science Symposium Conference Record (NSS/MIC), 2010 IEEE*, pages 2292–2293.
- [Smeets et al., 2012] Smeets, J., Roellinghoff, F., Prieels, D., Stichelbaut, F., Benilov, A., Busca, P., Fiorini, C., Peloso, R., Basilavecchia, M., Frizzi, T., Dehaes, J. C., and Dubus, A. (2012). Prompt gamma imaging with a slit camera for real-time range control in proton therapy. *Phys Med Biol*, 57(11):3371–3405.
- [Solevi et al., 2016] Solevi, P., Munoz, E., Solaz, C., Trovato, M., Dendooven, P., Gillam, J. E., Lacasta, C., Oliver, J. F., Rafecas, M., Torres-Espallardo, I., and Llosa, G. (2016). Performance of macaco compton telescope for ion-beam therapy monitoring: first test with proton beams. *Phys Med Biol*, 61(14):5149–5165.
- [Stichelbaut and Jongen, 2003] Stichelbaut, F. and Jongen, Y. (2003). Verification of the proton beam position in the patient by the detection of prompt gamma-rays emission. *Proceeding of the 39th PTCOG meeting, San Francisco*.

- [Testa et al., 2008] Testa, E., Bajard, M., Chevallier, M., Dauvergne, D., Le Foulher, F., Freud, N., Létang, J.-M., Poizat, J.-C., Ray, C., and Testa, M. (2008). Monitoring the bragg peak location of 73 mev carbon ions by means of prompt γ -ray measurements. *Applied Physics Letters*, 93(9):093506.
- [Testa et al., 2010] Testa, M., Bajard, M., Chevallier, M., Dauvergne, D., Freud, N., Henriquet, P., Karkar, S., Le Foulher, F., Létang, J. M., Plescak, R., Ray, C., Richard, M.-H., Schardt, D., and Testa, E. (2010). Real-time monitoring of the bragg-peak position in ion therapy by means of single photon detection. *Radiat Environ Biophys*, 49(3):337–343.
- [Todd et al., 1974] Todd, R. W., Nightingale, J. M., and Everett, D. B. (1974). A proposed γ camera. *Nature*, 251:132 EP –.
- [Toshito et al., 2010] Toshito, T., Bagulya, A., Lechner, A., Ivanchenko, V., Maire, M., Akagi, T., and Yamashita, T. (2010). New Geant4 electromagnetic physics developments for ion therapy applications. In *Proc. Int. Conf. On Supercomputing in Nuclear Applications and Monte Carlo (SNA+MC 2010)*, Tokyo, Japan.
- [Verbarg and Seco, 2014] Verbarg, J. M. and Seco, J. (2014). Proton range verification through prompt gamma-ray spectroscopy. *Phys Med Biol*, 59(23):7089–7106.
- [Weyrather et al., 1999] Weyrather, W. K., Ritter, S., Scholz, M., and Kraft, G. (1999). Rbe for carbon track-segment irradiation in cell lines of differing repair capacity. *Int J Radiat Biol*, 75(11):1357–1364.
- [Yoshihara et al., 2017] Yoshihara, Y., Shimazoe, K., Mizumachi, Y., Takahashi, H., Kamada, K., Takeda, A., Tsuru, T., and Arai, Y. (2017). Development of electron-tracking compton imaging system with 30- μ m soi pixel sensor. *Journal of Instrumentation*, 12(01):C01045.
- [Zoglauer et al., 2011] Zoglauer, A., Boggs, S. E., Galloway, M., Amman, M., Luke, P. N., and Marc Kippen, R. (2011). Design, implementation, and optimization of MEGAlib’s image reconstruction tool Mimrec. *Nuclear Instruments and Methods in Physics Research Section A: Accelerators, Spectrometers, Detectors and Associated Equipment*, 652(1):568–571.